Pseudouridylation defect due to *DKC1* and *NOP10* mutations causes nephrotic syndrome with cataracts, hearing impairment, and enterocolitis

Eszter Balogh[a,b,1], Jennifer C. Chandler[c,1], Máté Varga[a,d,1,2], Mona Tahoun[c,e,1], Dóra K. Menyhárd[f,g], Gusztáv Schay[a,h], Tomas Goncalves[i], Renáta Hamar[d], Regina Légrádi[a,b], Ákos Szekeres[b], Olivier Gribouval[j], Robert Kleta[k,l], Horia Stanescu[k,l], Detlef Bockenhauer[k], Andrea Kerti[a,b], Hywel Williams[m], Veronica Kinsler[n], Wei-Li Di[o], David Curtis[p], Maria Kolatsi-Joannou[c], Hafsa Hammid[c], Anna Szőcs[q], Kristóf Perczel[a,b], Erika Maka[r], Gergely Toldi[b], Florentina Sava[a], Christelle Arrondel[j], Magdolna Kardos[s], Attila Fintha[s], Ahmed Hossain[t], Felipe D'Arco[u], Mario Kaliakatsos[v], Jutta Koeglmeier[w], William Mifsud[x], Mariya Moosajee[y], Ana Faro[z], Eszter Jávorszky[a,b], Gábor Rudas[q], Marwa H. Saied[e], Salah Marzouk[e], Kata Kelen[b], Judit Götze[b], George Reusz[b], Tivadar Tulassay[b], François Dragon[t,aa], Géraldine Mollet[j], Susanne Motameny[bb], Holger Thiele[bb,cc], Guillaume Dorval[j], Peter Nürnberg[bb,cc], András Perczel[f,g], Attila J. Szabó[b,dd], David A. Long[c], Kazunori Tomita[i,ee], Corinne Antignac[j,ff], Aoife M. Waters[c,3,2], and Kálmán Tory[a,b,3,2]

[a]MTA-SE Lendület Nephrogenetic Laboratory, Semmelweis University, HU 1083 Budapest, Hungary; [b]First Department of Pediatrics, Semmelweis University, HU 1083 Budapest, Hungary; [c]Developmental Biology and Cancer Programme, University College London Great Ormond Street Institute of Child Health, WC1N 1EH London, United Kingdom; [d]Department of Genetics, Eötvös Loránd University, HU 1117 Budapest, Hungary; [e]Clinical and Chemical Pathology Department, Faculty of Medicine Alexandria University, EG 21500, Egypt; [f]MTA-ELTE Protein Modeling Research Group, Eötvös Loránd University, HU 1117 Budapest, Hungary; [g]Laboratory of Structural Chemistry and Biology, Eötvös Loránd University, HU 1117 Budapest, Hungary; [h]Department of Biophysics and Radiation Biology, Semmelweis University, HU 1085 Budapest, Hungary; [i]Chromosome Maintenance Research Group, University College London Cancer Institute, WC1E 6DD London, United Kingdom; [j]Laboratory of Hereditary Kidney Diseases, Imagine Institute, INSERM, UMR 1163, Université de Paris, FR 75015 Paris, France; [k]Division of Medicine, Royal Free Hospital, NW3 2QG London, United Kingdom; [l]Nephrology, Faculty of Medical Sciences, University College London, WC1E 6DE London, United Kingdom; [m]GOSgene, Experimental and Personalised Medicine, University College London Great Ormond Street Institute of Child Health, WC1N 1EH London, United Kingdom; [n]Genetics and Genomic Medicine, University College London Great Ormond Street Institute of Child Health, WC1N 1EH London, United Kingdom; [o]Infection, Immunity, Inflammatory, and Physiological Medicine, University College London Great Ormond Street Institute of Child Health, WC1N 1EH London, United Kingdom; [p]University College London Genetics Institute, University College London, C1E 6AD London, United Kingdom; [q]Medical Imaging Department, Neuroradiology Department, Semmelweis University, HU 1082 Budapest, Hungary; [r]Department of Ophthalmology, Semmelweis University, HU 1085 Budapest, Hungary; [s]Second Department of Pathology, Semmelweis University, HU 1091 Budapest, Hungary; [t]Département des Sciences Biologiques, Université du Québec à Montréal, Montréal, QC H2X 1Y4, Canada; [u]Department of Neuro-Radiology, Great Ormond Street Hospital, WC1N 3JH London, United Kingdom; [v]Department of Neurology, Great Ormond Street Hospital, WC1N 3JH London, United Kingdom; [w]Department of Gastroenterology, Great Ormond Street Hospital, WC1N 3JH London, United Kingdom; [x]Department of Histopathology, Great Ormond Street Hospital, WC1N 3JH London, United Kingdom; [y]Institute of Ophthalmology, University College London, EC1V 9EL London, United Kingdom; [z]Division of Biosciences, Department of Cell and Developmental Biology, University College London, WC1E 6BT London, United Kingdom; [aa]Centre d'Excellence en Recherche sur les Maladies Orphelines - Fondation Courtois, Université du Québec à Montréal, Montréal, QC H2X 1Y4, Canada; [bb]Cologne Center for Genomics, University of Cologne, DE 50931 Cologne, Germany; [cc]Center for Molecular Medicine Cologne, University of Cologne, DE 50931 Cologne, Germany; [dd]MTA-SE Pediatrics and Nephrology Research Group, HU 1083 Budapest, Hungary; [ee]Department of Life Sciences, Brunel University London, UB8 3PH, United Kingdom; and [ff]Assistance Publique–Hôpitaux de Paris, Hôpital Necker-Enfants Malades, Service de Génétique Moléculaire, FR 75015 Paris, France

Edited by Joan A. Steitz, Howard Hughes Medical Institute and Yale University, New Haven, CT and approved May 4, 2020 (received for review February 18, 2020)

RNA modifications play a fundamental role in cellular function. Pseudouridylation, the most abundant RNA modification, is catalyzed by the H/ACA small ribonucleoprotein (snoRNP) complex that shares four core proteins, dyskerin (DKC1), NOP10, NHP2, and GAR1. Mutations in *DKC1*, *NOP10*, or *NHP2* cause dyskeratosis congenita (DC), a disorder characterized by telomere attrition. Here, we report a phenotype comprising nephrotic syndrome, cataracts, sensorineural deafness, enterocolitis, and early lethality in two pedigrees: males with *DKC1* p.Glu206Lys and two children with homozygous *NOP10* p.Thr16Met. Females with heterozygous *DKC1* p.Glu206Lys developed cataracts and sensorineural deafness, but nephrotic syndrome in only one case of skewed X-inactivation. We found telomere attrition in both pedigrees, but no mucocutaneous abnormalities suggestive of DC. Both mutations fall at the dyskerin–NOP10 binding interface in a region distinct from those implicated in DC, impair the dyskerin–NOP10 interaction, and disrupt the catalytic pseudouridylation site. Accordingly, we found reduced pseudouridine levels in the ribosomal RNA (rRNA) of the patients. Zebrafish *dkc1* mutants recapitulate the human phenotype and show reduced 18S pseudouridylation, ribosomal dysregulation, and a cell-cycle defect in the absence of telomere attrition. We therefore propose that this human disorder is the consequence of defective snoRNP pseudouridylation and ribosomal dysfunction.

pseudouridylation | H/ACA snoRNP | pediatrics | telomere | rRNA

Author contributions: E.B., J.C.C., M.V., M.T., D.K.M., G.S., T.G., R.H., R.L., Á.S., O.G., R.K., H.S., D.B., A.K., H.W., V.K., W.-L.D., D.C., M.K.-J., H.H., K.P., G.T., F.S., C. Arrondel, A.H., F. D'Arco, M. Kaliakatsos, J.K., W.M., M.M., A. Faro, E.J., M.H.S., S. Marzouk, G.M., S. Motameny, H.T., D.A.L., K. Tomita, and K. Tory designed research; E.B., J.C.C., M.V., M.T., D.K.M., G.S., T.G., R.H., R.L., Á.S., O.G., R.K., H.S., D.B., A.K., H.W., V.K., W.-L.D., D.C., M.K.-J., H.H., K.P., E.M., G.T., F.S., C. Arrondel, M. Kardos, A. Fintha, A.H., F. D'Arco, M. Kaliakatsos, J.K., W.M., M.M., A. Faro, E.J., G. Rudas, M.H.S., S. Marzouk, J.G., G.M., S. Motameny, H.T., P.N., D.A.L., K. Tomita, and K. Tory performed research; M.V., G.S., Á.S., O.G., D.B., A.S., E.M., M. Kardos, A. Fintha, G. Rudas, T.T., F. Dragon, P.N., A.P., A.J.S., D.A.L., K. Tomita, C. Antignac, A.M.W., and K. Tory contributed new reagents/analytic tools; E.B., J.C.C., M.V., M.T., D.K.M., G.S., T.G., R.H., R.L., Á.S., O.G., R.K., H.S., D.B., A.K., H.W., V.K., W.-L.D., D.C., M.K.-J., H.H., A.S., K.P., E.M., G.T., F.S., M. Kardos, A. Fintha, A.H., F. D'Arco, M. Kaliakatsos, J.K., W.M., M.M., A. Faro, E.J., G. Rudas, M.H.S., S. Marzouk, K.K., J.G., G. Reusz, T.T., F. Dragon, G.M., S. Motameny, H.T., G.D., P.N., D.A.L., K. Tomita, C. Antignac, A.M.W., and K. Tory analyzed data; and E.B., J.C.C., M.V., M.T., D.K.M., G.S., R.L., Á.S., A.S., E.M., G.T., F. Dragon, P.N., D.A.L., K. Tomita, C. Antignac, A.M.W., and K. Tory wrote the paper.

The authors declare no competing interest.

This article is a PNAS Direct Submission.

Data deposition: Raw sequence data have been deposited in the Sequence Read Archive, https://www.ncbi.nlm.nih.gov/sra (accession no. PRJNA548449).

[1]E.B., J.C.C., M.V., and M.T. contributed equally to this work.

[2]To whom correspondence may be addressed. Email: mvarga@ttk.elte.hu, aoife.waters@gosh.nhs.uk, or tory.kalman@med.semmelweis-univ.hu.

[3]A.M.W. and K. Tory contributed equally to this work.

This article contains supporting information online at https://www.pnas.org/lookup/suppl/doi:10.1073/pnas.2002328117/-/DCSupplemental.

First published June 17, 2020.

Significance

Isomerization of uridine to pseudouridine is the most abundant RNA modification in eukaryotes. In ribosomal RNA (rRNA), this process of pseudouridylation is catalyzed by a ribonucleoprotein complex. Mutations of this complex were formerly identified in mucocutaneous and developmental abnormalities, resulting from telomere attrition. Here, we identified complementary mutations in two proteins of the complex, affecting the highly conserved pseudouridylation catalytic site, associated with a phenotype characterized by renal, ocular, intestinal, and auditory features, alongside reduced pseudouridine in rRNA and telomere attrition. Using a zebrafish model, we provide supporting evidence that this phenotype results from ribosomal dysfunction arising from a pseudouridylation defect of rRNAs. Together, this describes a phenotype associated with the disruption of the most abundant RNA modification.

Pseudouridylation, the isomerization of uridine (U) to pseudouridine (Ψ), is the most common modification of RNA. It can be catalyzed by single-protein pseudouridine synthases (PUSs) that act independently to recognize the substrate uridine or by the H/ACA small nucleolar ribonucleoprotein (snoRNP) complex (1, 2). Each complex is composed of a unique guide RNA and four core proteins, NOP10, NHP2, GAR1, and the catalytically active dyskerin (DKC1) (3). Knockdown of dyskerin results in a >50% reduction in ribosomal RNA (rRNA) pseudouridylation, indicating the primary role of the H/ACA snoRNP complex in the pseudouridylation of rRNAs (4).

Through its association with the telomerase RNA, *TERC*, the H/ACA snoRNP complex also plays a critical role in telomere synthesis (5). It is this function which links the snoRNPs [DKC1 (6, 7), NHP2 (8, 9), and NOP10 (10)] to the disease dyskeratosis congenita (DC; Online Mendelian Inheritance in Man [OMIM]: 305000, 224230, and 613987), characterized by mucocutaneous abnormalities and bone marrow failure, and its more severe form, Hoyeraal–Hreidarsson syndrome (HH), with intrauterine growth retardation, microcephaly, cerebellar hypoplasia, and, in rare cases, enteropathy. The role of defective telomere biogenesis in DC has been further corroborated by the identification of mutations in other genes, *TERT*, *TERC*, *TINF2*, and *RTEL1* (7, 11–14), which are implicated in telomere maintenance, but not in pseudouridylation. Indeed, progressive telomere attrition in the autosomal-dominant *TERT*- or *TERC*-related DC results in disease anticipation (15, 16), and wild-type (WT) offspring of telomerase-deficient mice with shortened telomeres develop an occult DC phenotype (17). The exhaustion of cellular renewal in *DKC1*-linked DC is rescued by the overexpression of *TERC*, reflecting the driving role of *TERC* level in the pathogenesis (18).

While human disorders associated with PUS-mediated pseudouridylation defects have been described (19–21), a human phenotype related to defective H/ACA snoRNP complex-mediated pseudouridylation has been lacking. Herein, we describe a human phenotype and early lethality in two unrelated pedigrees. By using linkage analysis and whole-exome sequencing, mutations within *DKC1* and *NOP10* were identified in two families. A combination of structural and in vivo analysis demonstrates that a pseudouridylation defect of rRNA is what drives the distinction of this phenotype from classic DC.

The two unrelated pedigrees presented with an infantile-onset disorder characterized by steroid-resistant nephrotic syndrome, cataracts (prior to steroid treatment), sensorineural deafness, and enterocolitis (Table 1 and Fig. 1). In the first pedigree, the disorder segregated in an X-linked pattern (Family A [FamA]; Fig. 1*V*) and in an autosomal recessive mode in the second (Family B [FamB]; Fig. 1*X*). All six affected males in FamA and the two affected females in FamB died in early childhood (Table 1). To identify the causative genetic loci, we performed linkage analysis in both families (Fig. 1 *W* and *Y*). A single locus of 5.1 Mb at the telomeric end of the X chromosome long arm segregated with the disease in FamA, assuming that the causative mutation led to germline mosaicism in I:2. By sequencing the locus-specific coding regions of the affected IV:14 and the haploidentical, but unaffected, II:9 males, we found a single difference in the sequences: a point mutation in *DKC1* (c.616 G>A, p.Glu206Lys; *SI Appendix*, Fig. S1*A*). We considered this variant to be causative, as it appeared de novo, segregated with disease in generation II corresponding to the assumed maternal germline mosaicism (Fig. 1*V*), affected a universally conserved glutamic acid (replaced by aspartic acid in some nonvertebrates; *SI Appendix*, Fig. S1*B*), and the resulting change to lysine was predicted to be pathogenic by Mutation Taster, Polyphen-2, and SIFT. This variant was absent in gnomAD and in 555 alleles of 368 ethnically matched controls. The mutation is thus classified as pathogenic based on the American College of Medical Genetics (ACMG)/Association for Molecular Pathology (AMP) criteria with evidence levels PS2, PM1-2, and PP1-3 (22).

In FamB, whole-exome sequencing and linkage analysis identified a mutation in *NOP10* (c.47C>T, p.Thr16Met; *SI Appendix*, Fig. S1*A*) within a homozygous region of 2.6 Mb in 15q14 (Fig. 1*Y*). The affected threonine is conserved down to yeast (*Saccharomyces cerevisiae*; *SI Appendix*, Fig. S1*B*); the change to methionine has not been found in the general population and was predicted as pathogenic by MutationTaster and SIFT. This variant is therefore also classified as likely pathogenic based on the ACMG/AMP criteria with evidence levels PM1-2, PP1, and PP3 (22).

There was minimal overlap between the DKC1 p.Glu206Lys-related and NOP10 p.Thr16Met-related phenotype (Figs. 1*L* and 2*H*) and the developmental anomalies of HH or the diagnostic mucocutaneous triad of DC (dyskeratosis, leukoplakia, and nail dystrophy) (7), though the latter typically appear between the ages of 5 and 10 y (23), beyond the lifetime of the children presented here (Table 1). Furthermore, with the exception of enterocolitis, cerebellar hypoplasia and progressive bone marrow failure found in a subset of the affected children (Table 1), the prominent features of this phenotype (Fig. 1 *D–U*), have not been reported in DC or HH. In contrast to the X-linked recessive transmission of *DKC1*-linked DC (24), females heterozygous for dyskerin p.Glu206Lys also developed cataracts and hearing impairment, necessitating artificial-lens implantation and hearing aids in the second decade of life (Fig. 1 and Table 1), as well as maxillary and mandibular hypoplasia, pigmentary retinopathy, microphthalmia, pineal hypoplasia, mild cerebellar vermis atrophy, and failure to thrive (Fig. 1, Table 1, and *SI Appendix*, Fig. S2). Pigmentary retinopathy was diagnosed in three heterozygous females (III:3, IV:4, and IV:12), resulting in no loss of visual acuity, but a flat electroretinogram. The index female in FamA (IV:4) developed a phenotype comparable to that of the males, requiring a hearing device at the age of 1 y, cataract operation at 5 y, and renal-replacement therapy by 6 y. However, no enterocolitis or bone marrow failure presented (up to her present age of 15 y). We found by allele-specific qPCR a highly skewed X-inactivation in skin cells and fibroblasts explaining her severe phenotype (Fig. 2*G*). In accordance with the survival advantage of the cells expressing the WT allele in *DKC1*-linked DC (25, 26), her X-inactivation in leukocytes tended to be skewed toward the mutant allele by the second decade of life (Fig. 2*G*).

We measured telomere length by Southern blot, monochrome multiplex quantitative PCR (MM-qPCR), and flow-fluorescent in situ hybridization (flow-FISH) and found the telomeres to be shortened in both families (Fig. 2 *A–F*), as with DC (27). This

Table 1. Clinical characteristics of the affected family members

Pt (sex)	Visual inv (age at first cat surgery)	Hearing impairment (age at HA)	Nephrotic syndrome (age at pres)	Enterocolitis (age at pres)	Other	Age at last follow-up/ death, y
Fam A						
II:1 (M)	Cat	nd	+	+ (infancy)	FTT	3*
II:3 (F)	–	+	–	–	–	60
II:8 (F)	Glau	+	–	–	–	58
II:1 (M)	Cat	nd	+	+ (6 mo)	BMF	2.5*
III:3 (F)	Cat (16 y), RP	+ (17 y)	–	–	HK, Mand, Max, MO, FTT	48
III:6 (F)	Cat (14 y)	+ (8 y)	–	–	CA, Mand, Max, PH, FTT	40
III:8 (F)	Cat (17 y)	+ (10 y)	–	–	FTT	45
III:11 (M)	nd	+	+	+ (6 mo)	FTT	4.5*
IV:1 (M)	Cat (2 y)	+ (2 y)	+ (>2 y)	+	–	2.5*
IV:4 (F)	Cat (4 y), RP	+ (1.5 y)	+ (2 y)	–	CA, MO, PH, FTT	15
IV:6 (M)	Cat (6 mos)	+ (6 mo)	+ (2.5 y)	+ (6 mo)	BMF, FTT	2.5*
IV:9 (F)	–	–	–	–	–	20
IV:12 (F)	Cat (10 y), RP	+	PU (10 y)	–	–	11
IV:14 (M)	Cat (3 y)	+ (3.5 y)	+ (2.5 y) FSGS	+ (5 y)	BMF, FTT	7.5*
IV:15 (F)	–	–	–	–	–	15
Fam B						
IV:3 (F)	Cat	+ (birth)	+ FSGS	+		3*
V:2 (F)	Cat	+ (birth)	+ MPGN	+	CH, HM	3*

BMF, bone marrow failure; CA, mild cerebellar atrophy; cat, cataracts; CH, cerebellar hypoplasia; F, female; FSGS, focal segmental glomerulosclerosis; FTT, failure to thrive; glau, glaucoma; HA, indication of hearing aid; HK, hyperkeratosis; HM, hypomyelination; inv, involvement; M, male; Mand, mandibular hypoplasia; Max, maxillary hypoplasia; MO, microphthalmia; MPGN, mesangial proliferative glomerulonephritis; nd, no data available; PH, pineal hypoplasia; pres, presentation; PU, nonnephrotic proteinuria; RP, retinitis pigmentosa.
*Age at death.

indicates that the identified mutations reduce the telomerase activity of the H/ACA snoRNP complex, similarly to other DC-related *DKC1* and *NOP10* mutations. However, as the phenotypic features could not be attributed to telomere shortening, we aimed to unravel what distinguishes the effect of these mutations from those associated with DC.

We first conducted structural analyses of the snoRNP complex. Dyskerin, NOP10, and NHP2 directly associate with the guide H/ACA small nucleolar RNA (snoRNA) (Fig. 3*A*), which binds and orientates the substrate RNA, specifically its target uridine, within the active pocket of dyskerin. Described cases of DC are associated with mutations that mostly concern amino acids implicated in the binding of the guide snoRNA (1, 28). The majority of these mutations are thus located at sites that interact with the guide RNA, such as the N or C termini of dyskerin (or Ser121 of the TruB domain), the Arg34 residue of NOP10—reported in the single family with a NOP10 mutation (10)—or Arg61, Pro87, and Val126 of NHP2 (Fig. 3*A*; spheres), with the only known exceptions of R158 and S280 of dyskerin. In contrast, dyskerin Glu206 and NOP10 Thr16 are located at the dyskerin–NOP10 interface, remote from both RNA components (Fig. 3*A*). We found the subcellular localization of the p.Glu206Lys dyskerin to be preserved, similar to the most common DC-related mutation, p.Ala353Val (*SI Appendix*, Fig. S3). Reciprocal coimmunoprecipitation analysis demonstrated that the complex formation capacity of p.Glu206Lys dyskerin–NOP10 and p.Thr16Met NOP10–dyskerin (Fig. 3*B*) was maintained. In native patient protein, where we observed a reduced level of p.Thr16Met NOP10, suggesting a possible effect on protein stability, the binding interaction with dyskerin was still maintained (*SI Appendix*, Fig. S4). However, both mutations did alter the hydrogen bonding (H-bonding) between dyskerin and NOP10, reflected in their dissociation constant, as reported by pressure-tuning fluorescence spectroscopy (Fig. 3 *C*–*F*) and the conformational changes (Fig. 3*G*) seen in molecular dynamics (MD) simulations (*SI Appendix*, Fig. S5). MD simulations of the WT and two mutant states of the human snoRNP complex (containing all four protein components, the guide- and substrate-RNA chains) were carried out by using homology modeling. The complex was modeled based on crystal-defined structures of full and partial H/ACA snoRNPs from *Pyrococcus furiosus* and *S. cerevisiae,* as the structure of the human enzyme complex has not yet been determined. Significantly, comparison of the MD-derived structures of the WT and mutant complexes revealed that structural changes at the dyskerin/NOP10 interaction surface resulted in a rearrangement of the pseudouridylation pocket (which sits over 20 Å away), detaching the catalytic Asp125 of dyskerin from the uridine of the bound substrate

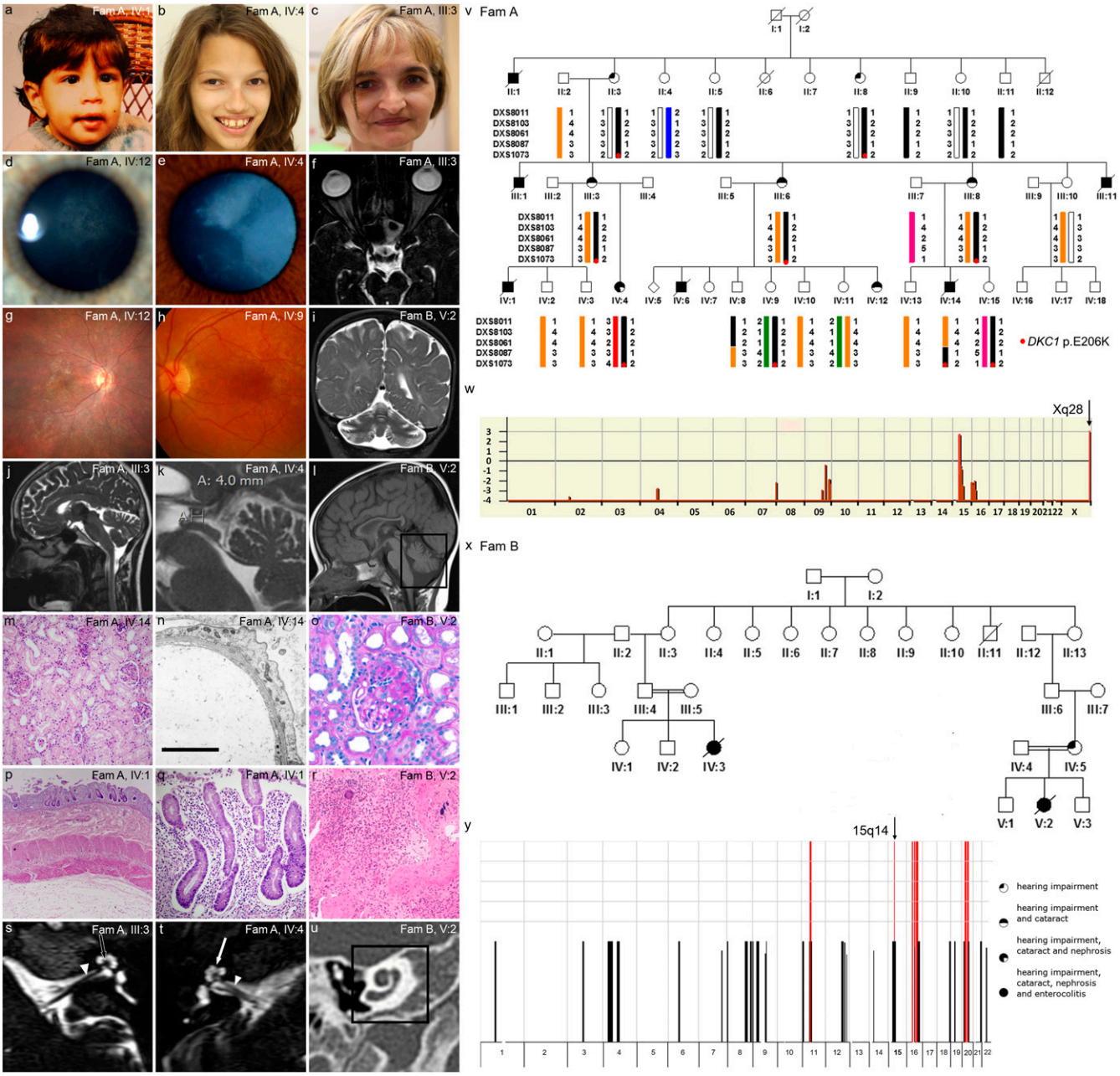

Fig. 1. Phenotype and genetic identification of the two affected families. (*A*–*C*) Affected males ($n = 6$) (*A*) and females ($n = 9$) (*B* and *C*) in FamA had no dysmorphic features apart from maxillary and mandibular hypoplasia in adult females. (*A*, *M*–*R*, and *V*–*X*) Affected males in FamA (*A*, *V*) and the two affected females ($n = 2$) from the consanguineous FamB (*X*) developed nephrotic syndrome with focal segmental glomerulosclerosis (*M*, *O*), diffuse podocyte foot process effacement (*N*), and enterocolitis with extensive chronic nonspecific inflammation (*P*–*R*). (*I* and *L*) In FamB, patient V:2, developed progressive hypomyelination (*I*) and cerebellar hypoplasia (*L*); both IV:3 and V:2 passed away in infancy. (*D*–*H*, *J*, *K*, and *S*–*U*) Cataracts (*D* and *E*) and sensorineural hearing impairment with a modiolus (*S*, black arrow; and *U*), cochlea (*T*, white arrow; and *U*) and cochlear nerve (*S* and *T*, white arrowheads) of normal morphology were present, even in the affected females of FamA, who had a normal lifespan and developed pigmentary retinopathy (*G* and *H*), microphthalmia (*F*), and pineal hypoplasia (*J* and *K*; *SI Appendix*, Fig. S2). (*V* and *W*) We found linkage to a 5.1-Mb region at Xq28 in the descendants of II:3 (*W*), assuming germline mosaicism in I:2 (*V*) with a LOD score of 3.01. (*V*) Through targeted sequencing in an unaffected and an affected but haploidentical male (II:9 and IV:14), we found a single de novo mutation in *DKC1* (c.616 G>A, p.Glu206Lys), which segregated among the six haploidentical members in the generation II with disease occurrence. (*X* and *Y*) Homozygosity mapping in FamB (*X*) showed a haploidentical homozygous region of 2.6 Mb at 15q14 with an LOD score of 3.03 (*Y*). Exome sequencing of patient V:2 and targeted segregation analysis of IV:3 and V:2, parents, and siblings revealed a homozygous missense mutation in *NOP10* (c.47C>T, p.Thr16Met). Scale bar in *N*: 3.5 μm.

RNA (Fig. 3*H*). Two different interaction paths can be found between the mutation sites and the catalytic core: one connecting Tyr15 of NOP10 to Arg248 of dyskerin, a residue that plays a role in fixing the phosphate group of the uridine substrate [via the Tyr15(NOP10)↔Arg247(dyskerin) H-bond] (29); and another intricate network of H-bonds and hydrophobic interactions linking the 16 to 18 segment of NOP10 and the loop 122 to 131 carrying the catalytic Asp125 of dyskerin: Thr16 and Lys18 of NOP10 form H-bonds with Glu206 and Glu208 of dyskerin, the latter of which is also H-bound to Arg211 (dyskerin). This residue is stacked against

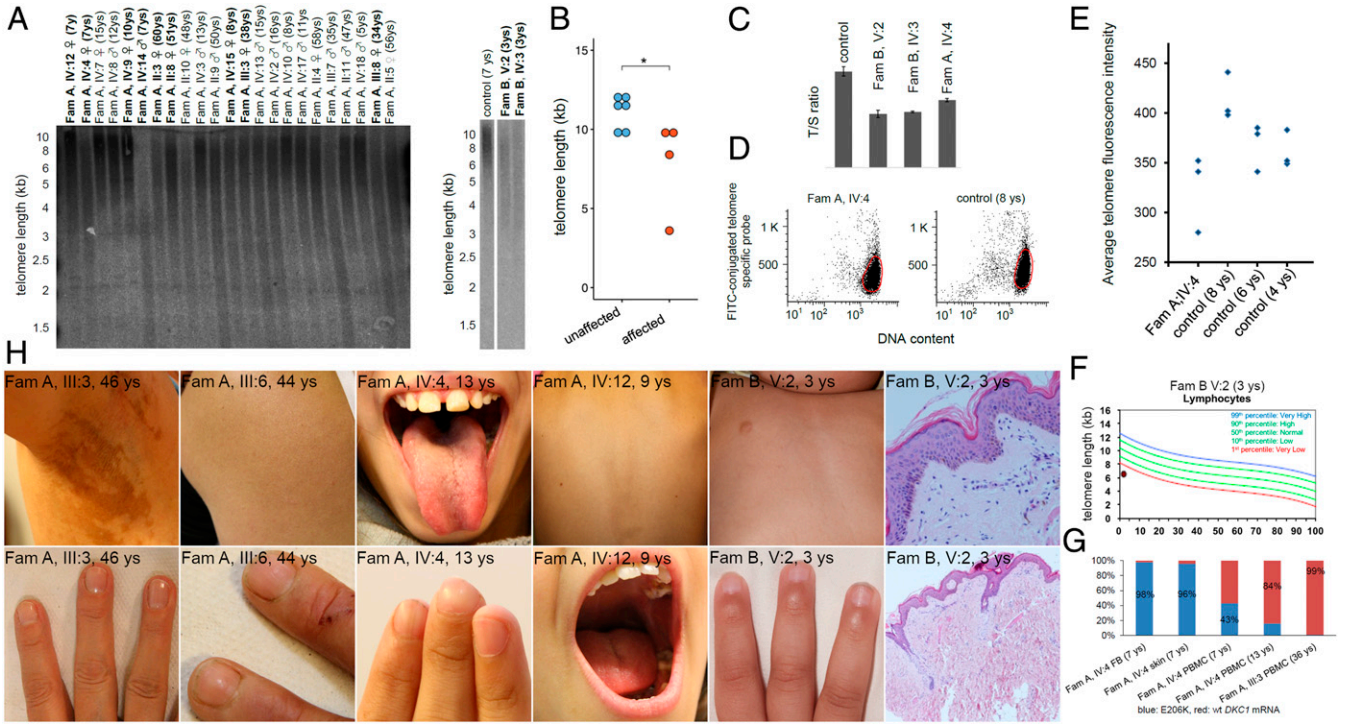

Fig. 2. Absent or subtle symptoms of DC despite telomere shortening. (*A* and *B*) We found telomere shortening in the affected individuals by Southern blot (heterozygous individuals in FamA and affected individuals in FamB are in bold) (*A*), showing a significant difference between the severely affected children (FamA, IV:4 and IV:14; FamB IV:3 and V:2) and six age-matched controls ($P = 0.038$) (*B*). (*C–F*) Telomere attrition was also shown by MM-qPCR as telomere copy number/standard copy number (T/S) ratio (*C*) and flow-FISH (*D–F*). (*G*) The severely affected index female (FamA, IV:4) showed a highly skewed X-inactivation in the fibroblasts and skin, with the ratio of her PBMCs expressing the mutant *DKC1* allele decreasing with age. FB, fibroblast. Blue, E206K; red, WT *DKC1* mRNA. (*H*) Despite telomere shortening, no nail dystrophy or leukoplakia was observed, with one heterozygous female from FamA (III:3) and one female from FamB (V:2) being diagnosed with mild dyskeratosis after genetic diagnosis. ys, years.

Phe2 of NOP10 that reaches into a pocket also comprising dyskerin Arg158, Leu213, Gln244, and Glu245. Glu245 is H-bound to His31 of NOP10, a residue also coordinated by Thr129 of dyskerin, which is located in the loop carrying the active Asp125. This gear-wheel-like contact surface of the two proteins allows for communication between far-lying sites; the subtle changes elicited by the mutations at the dyskerin/NOP10 interface therefore have the capacity to influence both substrate binding and catalysis in the substrate binding pocket of dyskerin. Together, these findings indicate that both dyskerin p.Glu206Lys and NOP10 p.Thr16Met alter the pseudouridylation capacity of the snoRNP complex, suggesting the pathogenic commonality underlying this phenotype.

As both mutations act by disrupting the catalytic center of dyskerin, we aimed to gain greater insight into the resulting pathogenesis and generated mutations in zebrafish *dkc1* targeting different regions of the gene (*elu1* and *elu8*; *SI Appendix*, Fig. S6). In situ hybridization characterized the expression of *dkc1* during zebrafish development, confirming its ubiquitous expression up to 12 h postfertilization (hpf), with strong expression at the sphere stage, suggesting the presence of a maternal component (*SI Appendix*, Fig. S7). Both *elu1* and *elu8* homozygous null *dkc1* mutants die at 5 days postfertilization (dpf) with a phenotype equivalent to the human phenotype. We confirmed the specificity of the null phenotype with a translation-blocking antisense morpholino (*SI Appendix*, Fig. S6).

Ocular sections of $dkc1^{elu1/elu1}$ larvae showed opaque lenses due to the persistence of nucleated fiber cells akin to zebrafish cataract models (30) and a high abundance of cells with a neuroepithelial morphology, characteristic of progenitor cells (Fig. 4*A*). We observed increased staining for proliferation markers in the retina and optic tecta (Fig. 4*A*), areas with high *dkc1* expression (*SI Appendix*, Fig. S7), indicative of a cell-cycle defect. Inner-ear development was impaired, with the cylindrical projections from the otocyst walls remaining unfused and the intestinal compartments of the gut undifferentiated (Fig. 4*B*). Indeed, several tissues showed reduced expression of differentiation markers in $dkc1^{elu1/elu1}$ larvae (Fig. 4*D*). Development of the pronephros was severely hypoplastic, with reduced Wt1-positive podocyte number (Fig. 4*B*), though no increased filtration of 500-kDa fluorescein isothiocyanate–dextran was observed at this stage (*SI Appendix*, Fig. S8*A*). A hematopoietic defect was also observed (Fig. 4*D* and *SI Appendix*, Fig. S8*C*), as described in previous *dkc1* and *nop10* null zebrafish models (31, 32). Lack of *dkc1* also caused defective jaw-cartilage development (*SI Appendix*, Fig. S8*B*) and a disorganized pineal gland (Fig. 4*C*), features of the female *DKC1* p.Glu206Lys patients (*SI Appendix*, Fig. S2).

Null mutants showed rescue with zygotic injection of WT human *DKC1* messenger RNA (mRNA) (Fig. 4*E* and *SI Appendix*, Fig. S6*D*). A far weaker rescue was achieved by *DKC1* p.Glu206Lys mRNA, indicating its pathogenicity with some limited function (Fig. 4*E* and *SI Appendix*, Fig. S6*D*). A hypomorphic (*elu2*) allele was also generated (*SI Appendix*, Fig. S6*A*): These $dkc1^{elu2/elu2}$ fish were viable, albeit with significant growth retardation (Fig. 5*J*). The combined analysis of two null mutants replicating the human phenotype, a morphant and the limited phenotypic rescue with *DKC1* p.Glu206Lys mRNA, provides strong support for the phenotypic relevance of this model.

Telomere biogenesis in the zebrafish is similar to that of humans (33). We observed no telomere shortening in the $dkc1^{elu1/elu1}$ animals (Fig. 5*A*), similar to *nop10* or *nola1* (*GAR1*)-deficient larvae (31, 32). Our structural analysis, demonstrating the effect of p.Glu206Lys and p.Thr16Met on the pseudouridylation pocket, suggested a potential role for the defective pseudouridylation of the rRNA and consequential ribosomal dysfunction. The abundance of processed 18S rRNA was low in $dkc1^{elu1/elu1}$ larvae (Fig. 5*B*), as with previous findings in *nop10* and *nola1*

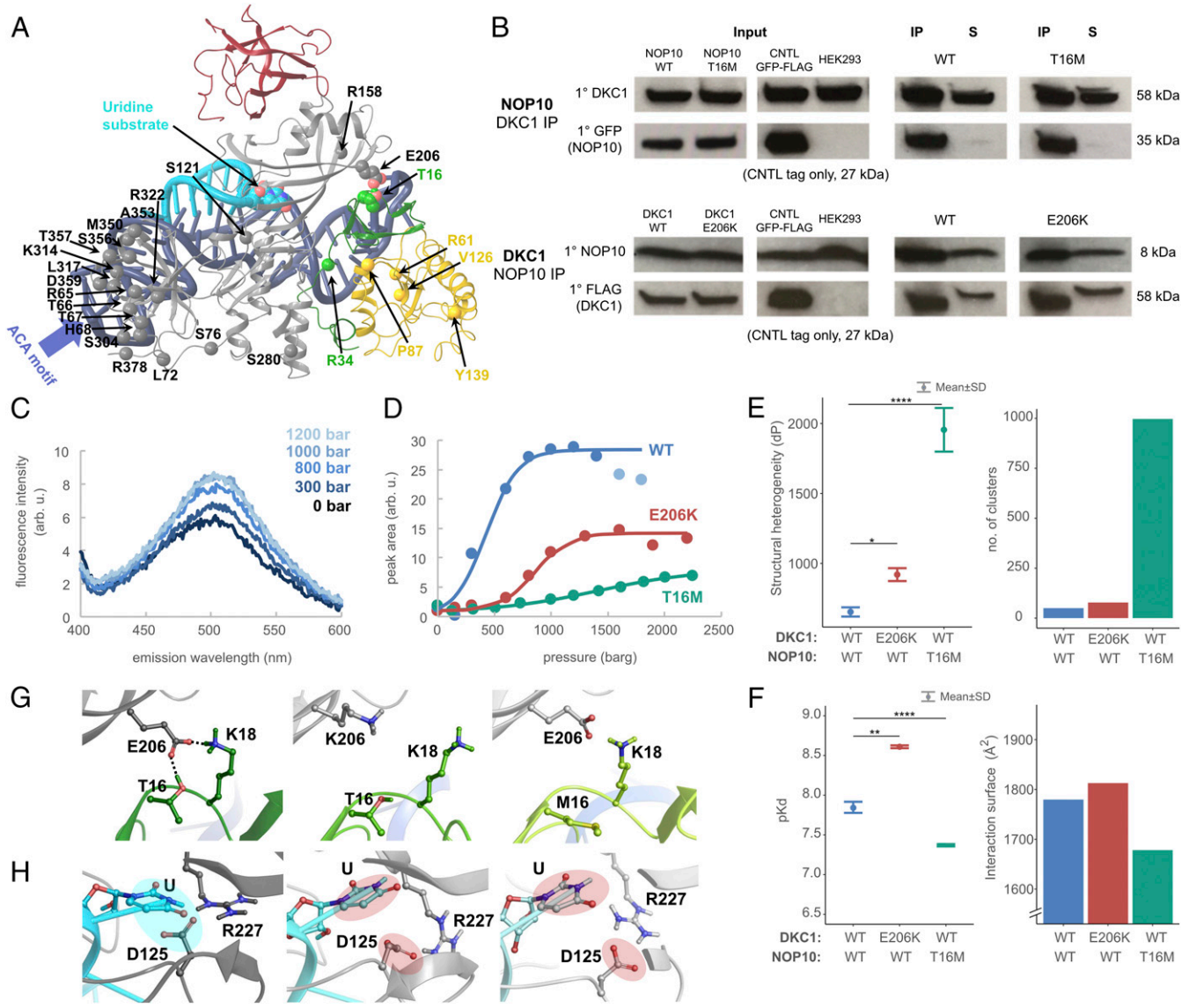

Fig. 3. Dyskerin p.Glu206Lys and NOP10 p.Thr16Met mutations alter the pseudouridylation pocket of the H/ACA snoRNP complex. (*A*) Homology modeling of human H/ACA snoRNP dyskerin (amino acids 60 to 380), gray; NOP10, green; GAR1, red; NHP2, yellow; guide snoRNA, dark blue; and substrate RNA, light blue. The Glu206 (dyskerin) and Thr16 (NOP10) are in CPK format (carbon atoms are shown in the color of the backbone, oxygen in red, and nitrogen in blue). The C-alpha atoms of residues associated with DC and HH syndrome are shown in spheres. (*B*) Coimmunoprecipitation of native dyskerin from HEK293 cells transfected with green fluorescent protein (GFP)-tagged WT and T16M NOP10 and reciprocal immunoprecipitation of native NOP10 from HEK293 cells transfected with Flag-tagged WT and E206K dyskerin. Immunoblots show that both mutant proteins immunoprecipitate with their native counterpart (see also *SI Appendix*, Fig. S4). CNTL, control. (*C* and *D*) Pressure-tuning fluorescence spectra of WT and mutant dyskerin–NOP10 complexes, where mutant complexes show an altered stability. Arb. u., arbitrary units; barg, bar in gauge. (*E*) Structural heterogeneity indicates significant structural difference between mutants and WT (Welch test: DKC1, $P = 1.8 \times 10^{-2}$; NOP10, $P = 4.04 \times 10^{-11}$). (*F*) Disassociation constants of WT and mutant complexes show both mutations cause a parallel change in pKd (*Left*; Welch test: DKC1, $P = 9.54 \times 10^{-3}$; NOP10, $P = 1.55 \times 10^{-7}$) and the interaction surface (*Right*). (*G* and *H*) Conformational changes induced by the mutations (*G*) WT dyskerin Glu206 interacts with the NOP10 Thr16–Leu17–Lys18 segment forming H-bonds (*Left*), these H-bonds are disrupted by both the dyskerin E206K (*Center*) and NOP10 T16M (*Right*) mutations. (*H*) The WT interaction (*Left*) between the substrate uridine and the catalytic D125 of dyskerin is uncoupled by both dyskerin E206K (*Center*) and NOP10 T16M (*Right*). 1 °, primary antibody; CNTL, cells transfected with empty expression plasmid, expressing GFP-Flag, size of 28 kDa; HEK293, nontransfected cells; IP, immunoprecipitated protein; S, supernatant. Statistical significance is denoted by asterisks. *$P < 0.05$; **$P < 0.01$; ****$P < 0.0001$.

(*GAR1*) mutants and *dkc1* morphants (31, 32). This is in accordance with the reduced pseudouridylation of 18S rRNA in *dkc1*$^{elu1/elu1}$ and *dkc1*$^{elu8/elu8}$ larvae (Fig. 5*C*), as well as in the peripheral blood mononuclear cells (PBMCs) of patient IV:3, FamB (Fig. 5*D*), as detected by immuno-Northern blot. A pseudouridylation defect was also apparent in the decreased Ψ/U ratio (detected by high-performance liquid chromatography [HPLC]-mass spectrometry [MS]) in the PBMCs of the index female with skewed X-inactivation (FamA, IV:4) (Fig. 5*E*). In contrast, pseudouridylation of 18S rRNA in the fibroblasts and the Ψ/U ratio in the skin of these patients was not different from that of controls (*SI Appendix*, Fig. S9), suggestive of the tissue-specific effect of *DKC1* mutations on pseudouridylation (34). The difference in the pseudouridylation defect may contribute to the differential survival advantage of the mutant allele in fibroblasts and PBMCs in the index girl (FamA, IV:4) (Fig. 2*G*).

Transcriptomic analysis of the *dkc1*$^{elu1/elu1}$ larvae also highlighted defects in ribosome biogenesis (Fig. 5*F*), and the mutant phenotype was recapitulated in WT embryos treated with the translational inhibitor cycloheximide (35) (*SI Appendix*, Fig. S6*C*). This observed phenotype is also highly reminiscent of that described in homozygous mutants of genes encoding ribosomal proteins (31, 36–38). Together, these results suggest ribosomal dysfunction to be a main driver of the phenotype.

In accordance with previous zebrafish models of ribosomopathies (31, 32, 38), we found dysregulated Tp53 expression in mutants. Western blot analysis suggested the stabilization and accumulation of Tp53 protein in mutants (Fig. 5*G*), in line with previous results from disrupted ribosomal biogenesis models (39). Further analysis, however, showed the transcription of the full-length isoform to be down-regulated and the truncated, anti-apoptotic *Δ113p53* isoform up-regulated (Fig. 5*H*). The latter isoform inhibits the classic Tp53-response in zebrafish (40), fitting with the sustained proliferative state we describe (Fig. 4*A*). However, the *dkc1*$^{elu1/elu1}$ phenotype was not rescued on a *tp53*-null background (Fig. 5*I*), with the exception of a partial rescue of hematopoiesis (*SI Appendix*, Fig. S8*C*), as has been reported in *dkc1*-deficient (31) and *nop10*-deficient (32) larvae. This indicates that the major phenotypic features observed upon loss of Dkc1 function are not mediated by Tp53.

Previous studies suggest a more fundamental role for the snoRNP complex than that of hematopoiesis or telomere maintenance alone: *Dkc1*-deficient mice die in utero (26), and *nop10* and *nola1*/*GAR1* mutant and *dkc1* morphant zebrafishes die at 5 to 10 dpf, all with normal telomere length (32, 33). Though reduced dyskerin expression in mice (41) and some DC-related *DKC1* mutations (34) were shown to affect rRNA pseudouridylation, other DC-related *DKC1* mutations did not (18, 42), or exerted only a subtle effect (4). Here, we show that mutations affecting the dyskerin–NOP10 interaction and the pseudouridylation pocket of the H/ACA snoRNP complex cause a phenotype with early lethality. Several nonclassical phenotypic features have been described in telomere biology disorders (43). This phenotype presents the features of nephrotic syndrome and cataracts which have not yet been reported to be associated with mutations in the H/ACA snoRNP complex.

Given the large number of the patients with H/ACA snoRNP complex-related disorders and the >70 identified *DKC1* mutations, the finding of a phenotype related to the H/ACA snoRNP complex might seem unexpected. However, none of the previous *DKC1* mutations affect the highly conserved pseudouridylation catalytic site and, instead, affect the N- and C-terminal dyskerin residues, which show low conservation or are even absent in the *P. furiosus* ortholog, Cbf5 (29). Given the fundamental role of the H/ACA snoRNP complex in development, reflected by the early lethality of the knockout animal models (26, 32, 33), alongside the lack of missense variants affecting the dyskerin catalytic site, or of *DKC1* and *NOP10* loss-of-function mutations in patients with telomeropathies, a severe phenotype related to disrupted pseudouridylation seems likely. This is corroborated by the pseudouridylation defect in *DKC1*-deficient cells (4), but no significant defect in DC (4, 18, 42).

We believe that the phenotype we describe is a recorded example of that more severe case. Although, at present, we only describe two families, the causality of these mutations has strong support in 1) the significant logarithm of odds to base 10 (LOD) scores; 2) the size of the *DKC1* family, allowing for the genetic tracing of the germline mosaic, de novo p.Glu206Lys mutation for three generations prior to the index case; 3) the well-characterized role of both mutated amino acids in the interaction of DKC1 and NOP10 (29); and 4) the shared functional pathophysiology of telomere shortening. Similar examples of pleiotropy have been described in the *CEP290* (44), *PMM2* (45, 46), *REN* (47, 48), and *LMNA* (49, 50) genes. Indeed, it is

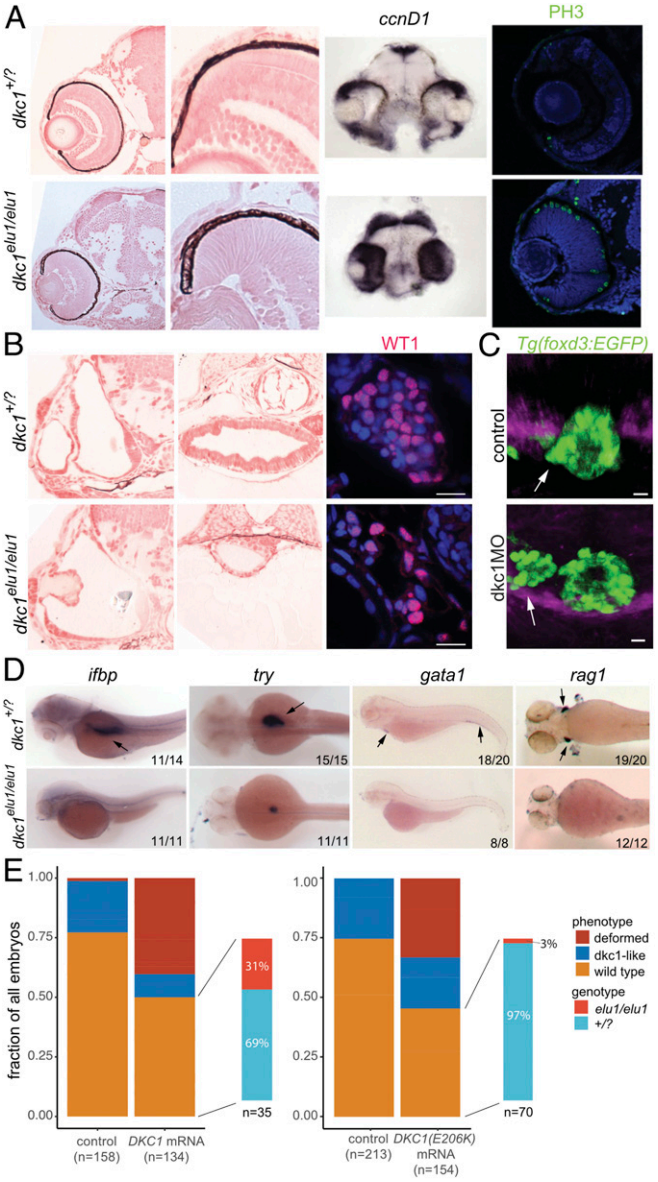

Fig. 4. The phenotype of *dkc1*$^{elu1/elu1}$ larvae recapitulates the human phenotype. (*A*) Histological analysis of *dkc1*$^{elu1/elu1}$ mutant larvae shows microphthalmia and cataracts. Both the eyes and the optic tectum of the mutants are abnormal and contain a high prevalence of cells with neuroepithelial character. Expression of cell-cycle markers *ccnD1* and PH3 in the retinae and the tecta of 2-dpf and 3-dpf larvae, respectively, can be observed throughout these tissues instead of being restricted to the proliferative regions of the ciliary marginal zone and the mediolateral edges, suggesting a defective cell cycle. (All pictures show coronal sections.) (*B*) Further histological analysis shows 1) deformed semicircular canals, 2) undifferentiated gut, and 3) hypoplastic pronephros with a reduced number of Wt1-positive podocytes in the mutant animals. (Scale bars: 10 μm.) (*C*) When Dkc1 function is abrogated in *Tg(foxd3:EGFP)* animals using a synthetic MO oligo, parapineal migration is impaired, and the pineal–parapineal complex appears immature at 3 dpf. (White arrows denote the parapineal.) (*D*) Markers of tissue differentiation demonstrate a lack of differentiation in the intestines (*ifbp*), pancreas (*try*), and the major blood lineages (*gata1* and *rag1*). (Black arrows denote area of expression.) (*E*) Injection of 1) human WT *DKC1* mRNA resulted in phenotypic rescue of the mutant larvae, as shown by the genotyping of larvae showing a WT phenotype. In contrast, injection of 2) human Glu206Lys *DKC1* mRNA elicited a much milder rescue, demonstrating the hypomorphic nature of this allele.

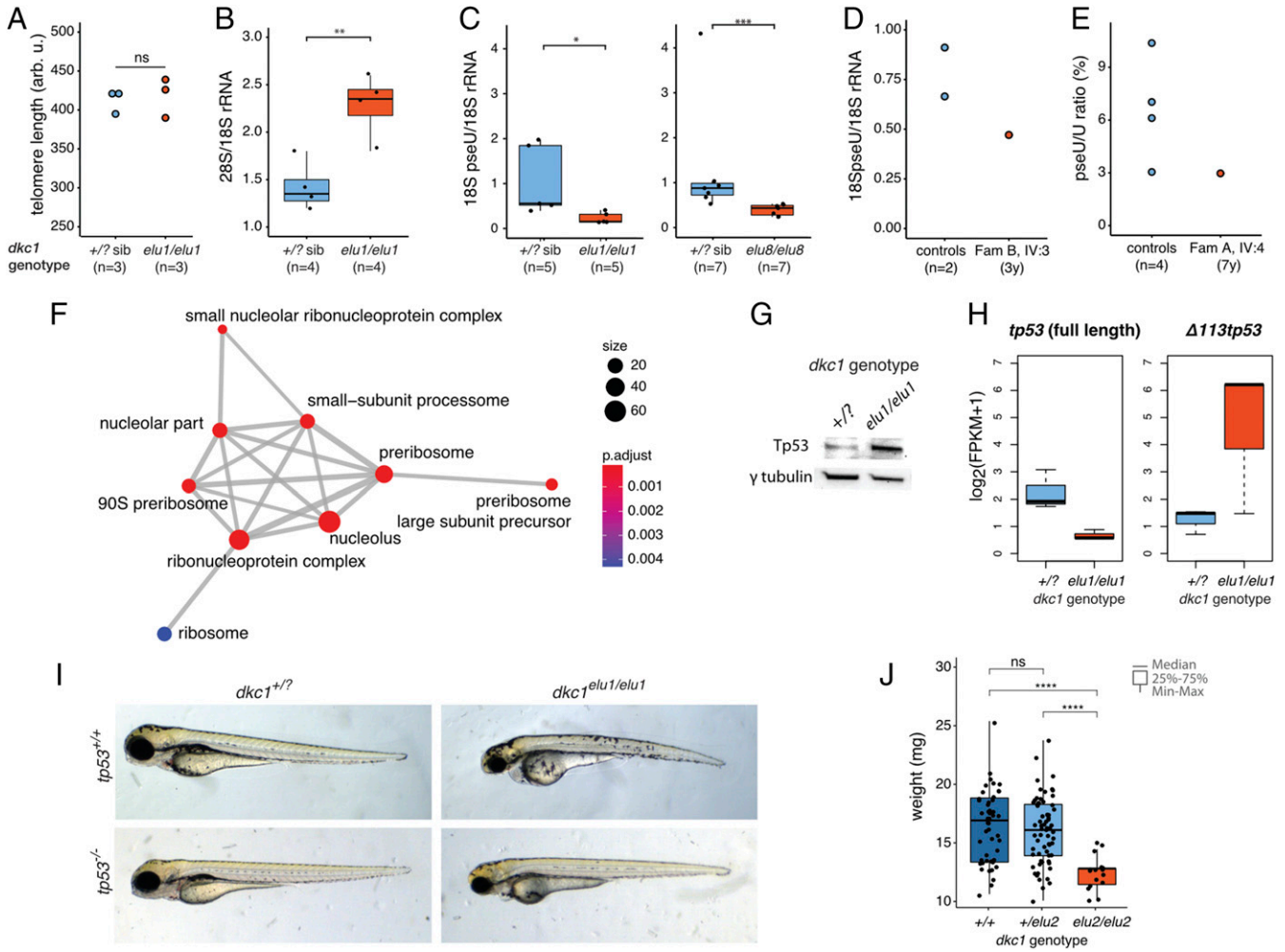

Fig. 5. Ribosomal dysfunction in *dkc1* zebrafish mutants due to defective pseudouridylation. (*A*) Telomere length is normal in *dkc1*$^{elu1/elu1}$ larvae at 4 dpf as measured by flow-FISH (n = 3 pooled samples of 10 larvae each, P = 0.7). Arb. u., arbitrary units; ns, not significant. (*B*) The 28S/18S rRNA ratio is increased in 4-dpf *dkc1*$^{elu1/elu1}$ larvae, suggesting impaired 18S rRNA processing (**P = 0.0033). (*C* and *D*) Immuno-Northern blot demonstrates a reduced pseudouridylation of 18S rRNA in *dkc1*$^{elu1/elu1}$, *dkc1*$^{elu8/elu8}$ 4-dpf larvae (+/? vs. *elu1/elu1*: *P = 0.016, +/? vs. *elu8/elu8*: ***P = 0.00058) (*C*) and in the leukocytes of patient FamB IV:3 (*D*). (+/?: heterozygous or homozygous WT fish.) (*E*) The female with skewed X-inactivation shows a decreased pseudouridine (pseU)/U ratio in the leukocytes, as determined by HPLC-MS. (*F*) Gene Ontology analysis of differentially regulated genes from 36 hpf *dkc1*$^{elu1/elu1}$ larvae demonstrates an up-regulation of genes associated with ribosome assembly and function. Size of the circles indicates the number of genes associated with certain terms, and color indicates the level of enrichment: red indicates high enrichment, and blue indicates low. P.adjust, adjusted *P*. (*G*) Western blot suggests the stabilization of Tp53 in the affected cells. (*H*) Transcriptomic analysis shows that the truncated, antiapoptotic *tp53* isoform (Δ 113p53) is up-regulated in mutants, while the canonical, full-length, proapoptotic isoform shows decreased expression; measured as fragments per kilobase of exon model per million reads mapped. (*I*) The phenotype of the *dkc1*$^{elu1/elu1}$ zebrafish mutants is Tp53-independent, as it is not rescued on a *tp53*$^{-}$ background. (*J*) Homozygous carriers of the missense (c.567_568insGTG) hypomorphic allele (*dkc1*$^{elu2/elu2}$) are viable, but show significant growth retardation compared with their siblings (n = 130) (+/+ vs. *elu2/elu2*: ****$P = 1.9 \times 10^{-9}$; +/*elu2* vs. *elu2/elu2*: ****$P = 1.6 \times 10^{-9}$). *$P < 0.05$; **$P < 0.01$; ***$P < 0.001$; ****$P < 0.0001$.

unlikely that this phenotype represents the most severe of the H/ACA snoRNP complex syndromes. Loss-of-function mutations are expected to result in an even more severe, potentially in-utero-lethal disorder, making the pleiotropy of the H/ACA snoRNPs even more pervasive.

Although telomere shortening was apparent, the disorder was lethal before the potential appearance of classic DC symptoms. Since the *dkc1* mutant zebrafish recapitulated the human phenotype with normal telomere length, but ribosomal dysfunction, a consequence of impaired 18S rRNA pseudouridylation, a feature also observed in the patients, we conclude that a pseudouridylation defect is the principal driver of this phenotype. Given the fundamental role of H/ACA snoRNP complex in targeting uridines not just in rRNAs, but also in small nuclear RNAs and mRNAs (1, 4, 51, 52), the varied site-specific impact felt on each uridine residue (34) and the additive consequences of the altered dyskerin–NOP10 interaction we describe, this phenotype may culminate from a pseudouridylation defect implicating multiple RNAs. There is increasing evidence for the broader pathogenicity of defective RNA processing in human pathologies (53). Mutations in the KEOPS (kinase, endopeptidase, and other proteins of small size) complex, involved in the modification of transfer RNAs, have recently been identified in Galloway–Mowat syndrome (54), and a role for defective rRNA methylation has now been described in DC (55). The findings presented here propose that defective pseudouridylation is a new mechanism for injury in the human kidney, eye, and cochlea, adding to our understanding of RNA processing in human disease.

Materials and Methods

Identification of the Causal Mutations. All patients or their legal representatives gave written informed consent, and the study was approved by the Local Research Ethic Committees (National Scientific and Ethical Committee of Hungary: TUKEB 1154/0-2010-1018EKU; and Institute of Child Health/Great Ormond Street Hospital Research Ethics Committee: 05/Q0508/6). For FamA, linkage analysis was performed by using the Human Mapping 250-k NspI array (Affymetrix), and parametric LOD scores were calculated with Multipoint Engine for Rapid Likelihood Interference software (56), assuming X-linked inheritance. Females with an uncertain phenotype in generation IV were not included in the linkage analysis. Extended haplotype analysis using five microsatellite markers (DXS8011, DXS8103, DXS8061, DXS8087, and DXS1073) flanking the *DKC1* locus was performed in all of the available members of FamA. PCR products with fluorescent primers were separated by capillary electrophoresis (3130 Genetic Analyzer) and analyzed by using GeneMapper analysis software (Life Technologies).

In the affected individual IV:14 and the haploidentical but unaffected individual II:9 of FamA, enrichment of the linkage interval (Xq28–Xqter:150,474,451 to 155,270,560 bp; GRCh37/hg19) and subsequent sequencing were performed as described (57). In brief, we used the Roche NimbleGen 385 K custom sequence capture array with a capacity of up to 5 Mb of target sequence. The exon-based design included all exons of the protein-coding genes, including 100 bp of flanking intron sequence and 1 kb of the promoter regions and known microRNAs within the critical interval. Final coverage of the design was 99.2%. Enrichment factors of >700-fold were achieved for the two samples. From the enriched DNA samples, we generated paired-end libraries and sequenced them on an Illumina GA IIx device with a read length of 2 × 36 bp. The average coverage of the 447,699 bp of target sequences was >360× in both samples. For data handling and analysis, we used our in-house database and analysis tool kit VARBANK (Version 2.0) (https://varbank.ccg.uni-koeln.de/varbank2/) with default settings for variant filtering. These parameters guarantee to focus on rare high-quality variants altering the protein sequence or showing impairments of splice and translation initiation sites. Only one such variant was found in the affected individual that was absent from the unaffected one, namely, *DKC1*:c.616G>A, p.Glu206Lys. The median of 31 pathogenicity rank scores calculated for this variant was 0.83, thus strongly supporting causality. The segregation of the *DKC1* variant was validated by Sanger sequencing.

For FamB, whole-exome sequencing of the first index patient (V:2) was conducted by GOSgene (BGI), from genomic DNA (gDNA) extracted from peripheral blood; exome capture was performed by using the Agilent SureSelect (Version 4) (51 Mb). Homozygosity mapping of candidate variants was conducted on index patients (V:2 and IV:3), parents, and siblings via Sanger sequencing. Segregation analysis confirmed an autosomal recessive mode of inheritance for a mutation in *NOP10* (c.47C>T, p.Thr16Met). This was confirmed through linkage analysis by using the Cyto SNP Microarray technique and Infinium assay HD Ultra kit (Illumina, catalog no. WG-901-4007). Sequencing files were assembled in Genome Studio, and regions of shared homozygosity were analyzed in Homozygosity Mapper.

Telomere Length Analysis. Three independent methods were used to assay the length of the telomeres: Southern blot, MM-qPCR, and flow-FISH (*SI Appendix*).

X-Inactivation Measurements. RNA was isolated from peripheral blood (NucleoSpin RNA Blood, Macherey-Nagel), skin, and fibroblasts (Total RNA Mini Kit Tissue, Geneaid) and was reverse-transcribed (catalog no. BIO-65042, Bioline; catalog no. K1671, Thermo Scientific) following the manufacturer's instructions. The X-inactivation ratio was assessed by allele-specific qPCR using a Taqman probe (LightCycler TaqMan Master, Roche; *SI Appendix*, Table S1). A dilution series of Flag-tagged WT and E206K *DKC1* plasmids were used for standardization; all measurements were performed three times.

Homology Modeling and MD Simulations. Homology models for the WT and mutant H/ACA snoRNP complexes were constructed based on full (4 proteins and both guide and substrate RNA) and partial H/ACA snoRNP complexes from *P. furiosus* and *S. cerevisiae* [Protein Data Bank (PDB) ID code 3hay (58), 3hjw (59), 3lwq (60), 2lbw (61), and 3u28 (62)] by using the Schrödinger Modeling Suite (63) and then subjected to 600-ns MD simulations by using GROMACS (64), with the AMBER-ff99SBildnp* forcefield (65) and the parametrization of Steinbrecher et al. (66) for the phosphate moieties. The simulations were solvated by ∼35,880 OPC (optimal three-charge, four-point rigid) water molecules (67), the total charge of the system was neutralized, and the physiological salt concentration was set by using Na^+ and Cl^- ions. Energy minimization of starting structures was followed by relaxation of constraints on protein atoms in three steps, with an additional constant number, volume, and temperature step (all of 200 ps) to stabilize pressure. Trajectories of 600-ns constant number, pressure, and temperature simulations at 325 K (to enhance sampling) and 1 bar were recorded for further analysis (collecting snapshots at every 4 ps). Clustering of the equilibrium trajectory was carried out based on the backbone structure of the interaction surface of dyskerin and NOP10 (containing the entire NOP10 model and residues of dyskerin that have an atom reaching within 6 Å of NOP10) using a 1 Å cutoff.

Coimmunoprecipitation Studies. Total protein was harvested by using the Pierce IP Lysis Buffer (Thermo Fisher, catalog no. 87787), and protein concentration was determined by using the BCA Protein Assay Kit (Thermo Fisher, catalog no. 23225). One milligram of protein lysate was incubated with 4 μg of target antibody for 8 h at 4 °C, followed by an overnight incubation with Dynabeads Protein G (Thermo Fisher, catalog no. 10003D). Immunoprecipitated samples were subject to immunoblot, and signal was detected by using Pierce enhanced chemiluminescence Western Blotting Substrate (Thermo Fisher, catalog no. 32106). In addition, primary keratinocytes were isolated from skin biopsy and cultured as described in Nowak et al. (68). Coimmunoprecipitation studies were conducted as described above with the amendment of 500 μg of protein lysate, 2 μg of NOP10 antibody (Abcam, catalog no. ab134902), and host-specific sheep anti-rabbit IgG Dynabeads (Invitrogen, catalog no. 11203D).

Protein Extraction for Pressure-Tuning Fluorescence Spectroscopy. Total protein was harvested by 150 mM NaCl, 20 mM Tris, and 1% Triton X supplemented with 0.1% protease inhibitor (Protease Inhibitor Cocktail, Sigma-Aldrich). Lysates were incubated with monoclonal anti-Flag (catalog no. F3165, Sigma-Aldrich) or anti-V5/NOP10 (catalog no. ab182008/ab134902, Abcam) Antibodies) and subsequently with Protein G beads (Dynabeads Protein G for Immunoprecipitation, Thermo Fisher Scientific). Dyskerin and NOP10 variants were eluted by competition with Flag and V5 peptides (catalog nos. B23111 and B23511, Biotool; catalog no. F3290, Sigma-Aldrich) for 30 min, repeated five times. Eluate concentration was measured by spectrophotometry (DC Protein Assay, Bio-Rad) and verified by sodium dodecyl sulfate/polyacrylamide gel electrophoresis, using anti-V5/anti-NOP10 (catalog no. F3165, Sigma Aldrich; catalog no. ab182008/ab134902, Abcam) as primary and anti-mouse/anti-goat immunoglobulin G (IgG)-horseradish peroxidase (HRP) as secondary (catalog nos. sc-2005 and sc-2357, SCBT) antibodies.

Pressure-Tuning Fluorescence Spectroscopy. Pressure-tuning fluorescence spectroscopy was used to determine the dissociation constant of the NOP10–dyskerin complex (K_d) and the pKd (pKd = −log(K_d)) (69, 70) as well as the volume change accompanying dissociation (ΔV, mL/mol). Briefly, the method involved the use of a fluorescent dye which binds to the solvent-accessible, hydrophobic regions of proteins; hydrostatic pressure was then varied to induce dissociation. By fitting a dissociation model to the fluorescence data, the K_d and ΔV values are determined as follows:

$$I(p) = I_0 + \Delta I \cdot \frac{\sqrt[2]{K_d^2 e^{-2\frac{p\Delta V}{RT}} + 16CK_d e^{-\frac{p\Delta V}{RT}}} - K_d e^{-\frac{p\Delta V}{RT}}}{8C},$$

where $I(p)$ and I_0 are the resulting and original fluorescence intensities, respectively; ΔI is the maximal intensity change; and C is the total protein concentration. This method yields a specific volume, and by determining the width of pressure range in the 5 to 95% dissociation regime, structural heterogeneity was qualitatively assessed. A nonlinear least squares was fitted to the data, and statistical difference between WT and mutant complexes was assessed via a Welch test (Statistica, Version 13.4). The interaction surface was directly related to the pKd through the general concept of the equilibrium constant:

$$K = A \cdot e^{-\frac{\Delta E}{kT}} = A \cdot e^{-\frac{aS_i + b}{kT}},$$

where ΔE is the complex formation energy, A is the pre-exponential factor, S_i is the interaction surface in square Ångströms (Å^2), and a, b are the parameters of the linear function connecting ΔE and S.

Generation of Zebrafish Mutants. CRISPR/Cas9-mediated mutagenesis of the *dkc1* gene was carried out in the WT *tuebingen* (*tue*) strain as described (71); targeted regions (guide RNA sequences) are listed in *SI Appendix*, Table S1.

Genotyping was conducted by using PCR on gDNA samples isolated from fin clips; the allele-specific forward primers for genotyping, sequencing of exons 7 and 11, and exon-specific reverse primers are listed in *SI Appendix*, Table S1. An antisense, translation-blocking morpholino (MO) was ordered from GeneTools to confirm specificity of the null *elu1* and *elu8* phenotypes. WT (*tue*) and mutant *dkc1* and *tp53* fish lines were maintained in the animal facility of Eötvös Loránd University according to standard protocols (72, 73). All zebrafish protocols were approved by the Hungarian National Food Chain Safety Office (Permit XIV-I-001/515-4/2012) and the Pest County Governmental Office (Permit Number: PE/EA/2023-7/2017).

Zebrafish Rescue Experiments. The coding sequences for human *DKC1* and *DKC1* E206K were cloned into a pCS2+ vector, linearized with *KpnI*, and in vitro-transcribed by using the mMessage mMachine SP6 kit (Ambion). Zebrafish embryos from a $dkc1^{elu1/+}$ in-cross were injected with *DKC1* mRNA at the one- to two-cell stage and phenotypically scored at 4 dpf.

Zebrafish Histology. In situ hybridization experiments, Neutral Red, and hematoxylin–eosin histological stainings, immunostaining, Acridin Orange labeling, and filtration tests using fluorescent dextrans were performed according to standard protocols (*SI Appendix*).

Zebrafish Growth Measurements. Offspring of in-crossed $dkc1^{elu2/+}$ heterozygous fish were housed and raised at standard stocking densities. Measurements were taken at 4 mo of age. Body length was measured as standard length, from the tip of the head to the end of the trunk, and wet body weight was determined by using a standardized method (74), to avoid anesthesia.

Analysis of 28S/18S rRNA Ratio and Pseudouridylation. Total RNA was isolated from 4.5 to 5 dpf zebrafish by the TRIzol Reagent (Invitrogen). The RNA quality was assessed on an Agilent 2100 Bioanalyzer by using the RNA 6000 Pico kit (Agilent Technologies), according to the manufacturer's instructions. For comparison of 18S and 28S rRNA abundance in mutant and WT fish, densitometry of the 18S and 28S peaks was performed by using ImageJ, and their ratio was compared by Student's *t* test (Statistica software, Version 13.2).

Pseudouridylation was assessed by immuno-Northern blotting as described (75). In brief, 3 μg of total RNA was loaded per well on a 1.5% denaturing agarose gel and imaged to assess for degradation. Gel blotting was performed overnight onto a nylon membrane (Amersham Hybond-N, GE Healthcare Life Sciences), followed by ultraviolet cross-linking. Nylon membranes were blocked with 5% nonfat milk for 1 h, then incubated with an anti-pseudouridine (D-347-3, MBL, diluted [dil.] 1:500 in phosphate-buffered saline [PBS]) primary antibody for 1.5 h, followed by an HRP-conjugated anti-mouse IgG (sc-2005, SCBT; dil. 1:1,000 in PBS) secondary for 1 h, all at room temperature. Bands were visualized by chemiluminescence (Western Blotting Luminol Reagent, sc-2048, SCBT) on a Molecular Imager VersaDoc MP 5000 System (Bio-Rad). Densitometry was performed by using the ImageJ processing program. Experiments were repeated three times. To assess the 18S rRNA pseudouridylation, the ratio of the normalized 18S rRNA pseudouridine, and the normalized 18S rRNA was compared between the mutant and the sibling zebrafish by Mann–Whitney *U* test.

Whole-Transcriptome Analysis. Total RNA was extracted from whole zebrafish embryos at 36 hpf by using TRIzol reagent (Thermo Fisher, catalog no. 15596018), and three biological replicate samples were prepared for mutants and siblings, respectively. The samples were sequenced on the Illumina MiSeq platform by Microsynth (Microsynth AG), according to standard Illumina protocols. Raw sequence data were deposited to the Sequence Read Archive (SRA), accession no. PRJNA548449. Raw reads were preprocessed with FASTQC (76), followed by analysis based on the "new tuxedo pipeline" (HISAT, StringTie, and Ballgown) using default settings (77). Gene Ontology term analysis and visualization was performed by using the emapplot function of the clusterProfiler package (78).

Determination of Pseudouridine and U Content Via HPLC-MS. RNA was isolated from peripheral blood (NucleoSpin RNA Blood, Macherey-Nagel) and skin (Total RNA Mini Kit Tissue, Geneaid), and their pseudouridine and U content were measured as described (79). Briefly, for the determination, an HPLC-tandem MS system was used, including an Agilent 1100 modular HPLC (Agilent Technologies) and an MDS Sciex API 4000 Triple-Quad mass spectrometer (Applied Bioscience) equipped with the TurboV-Spray source. For the gradient elution on the Phenomenex Luna C 18, 5 μm × 3.0 mm × 150 mm column (Gen-Lab), water (A), and a mixture of water and methanol (50% volume [V]/V, B) were used, both supplemented with ammonium acetate (25 mM). At the initial stage of the separation, the B was kept at 0% for 1 min and increased up to 100% for 5 min, which was held for 3 min before the column equilibration. The flow rate was 400 μL/min, and the column was thermostated at 55 °C. For the detection, the mass spectrometer operated in the positive mode, where the electrospray ionization ion source gas temperature was set at 525 °C, the ionization voltage at 5,000 V. During the multiple reaction-monitoring measurements, the precursor ion was set to *m/z* 245.2, while the monitored fragment ion was *m/z* 113.1, using 50 V and 20 eV for the declustering potential and collision energy, respectively.

Data Availability Statement. All relevant data are included in the main text and *SI Appendix*. Zebrafish transcriptomic datasets generated for this study can be found in the National Center for Biotechnology Information SRA (accession no. PRJNA548449).

Web Resources. URLs for data and resources presented herein are as follows: BIOPKU, www.biopku.org/home/home.asp; Ensembl, https://www.ensembl.org/index.html; gnomAD, https://gnomad.broadinstitute.org/; the Human Gene Mutation Database, www.hgmd.cf.ac.uk/ac/index.php; the Human Genome Variation Society, https://varnomen.hgvs.org; the Leiden Open Variation Database, https://www.lovd.nl/3.0; Mutalyzer, https://mutalyzer.nl/; Mutation Taster, www.mutationtaster.org/; OMIM, www.omim.org/; PolyPhen-2, genetics.bwh.harvard.edu/pph2/; and Sorting Intolerant from Tolerant, https://sift.bii.a-star.edu.sg/.

ACKNOWLEDGMENTS. We thank Rózsa Csohány, Mária Bernáth, Dániel Silhavy, Kata Gyulay, Noémi Borbély, Mirjam Pencz, Zoltán Varga, and Julianna Víg for their help and Moin Saleem for providing the podocyte cell line. This work was supported by Hungarian Academy of Sciences MTA-SE Lendulet Research Grant LP2015-11/2015; Pfizer's Research Grant; Zoltán Magyary and the National Research, Development and Innovation Office grants K109718, and KH125566 (to K. Tory); and K116305 (to D.K.M.); the Ministry of Human Capacities in Hungary in the frame of Institutional Excellence Program for Higher Education, Hungarian National Research, Development and Innovation Office Grant NRDI-FK124230, New National Excellence Program Grant ÚNKP-17-4, and Eötvös Loránd University Institutional Excellence Program Grant 1783-3/2018/FEKUTSRAT (to M.V.); a MedinProt Synergy IV grant (to M.V. and G.S.); for the Development of the Scientific School of physicians, healthcare personnel and pharmacists Grant EFOP-3.6.3-VEKOP-16-2017-00009 from the European Social Fund and the Hungarian State (to E.B.); Medical Research Council Clinician Scientist Fellowship MR/K010654/1 (to A.M.W.); Kidney Research UK Innovation and Project Grant Paed_RP_011_20170929 and the National Institute for Health Research Biomedical Research Centre at Great Ormond Street Hospital for Children National Health Service Foundation Trust and University College London (to A.M.W., J.C.C., and D.A.L.); an Egyptian Cultural Affairs and Mission Sector, Ministry of High Education grant (to M.T.); Cancer Research UK Grant C36439/A12097 (to K. Tomita); and a Chercheur-boursier Award of the Fonds de Recherche en Santé du Québec and a grant from the Natural Sciences and Engineering Research Council of Canada RGPIN 249792 (to F. Dragon). We thank the National Information Infrastructure Development Institute (NIIFI) supercomputing center (Hungary) for providing computational facilities.

1. A. M. Kiss, B. E. Jády, E. Bertrand, T. Kiss, Human box H/ACA pseudouridylation guide RNA machinery. *Mol. Cell. Biol.* **24**, 5797–5807 (2004).
2. M. Penzo, L. Montanaro, Turning uridines around: Role of rRNA pseudouridylation in ribosome biogenesis and ribosomal function. *Biomolecules* **8**, E38 (2018).
3. M. Khanna, H. Wu, C. Johansson, M. Caizergues-Ferrer, J. Feigon, Structural study of the H/ACA snoRNP components Nop10p and the 3′ hairpin of U65 snoRNA. *RNA* **12**, 40–52 (2006).
4. S. Schwartz *et al.*, Transcriptome-wide mapping reveals widespread dynamic-regulated pseudouridylation of ncRNA and mRNA. *Cell* **159**, 148–162 (2014).
5. K. Collins, J. R. Mitchell, Telomerase in the human organism. *Oncogene* **21**, 564–579 (2002).
6. N. S. Heiss *et al.*, X-linked dyskeratosis congenita is caused by mutations in a highly conserved gene with putative nucleolar functions. *Nat. Genet.* **19**, 32–38 (1998).
7. I. Dokal, T. Vulliamy, P. Mason, M. Bessler, Clinical utility gene card for: Dyskeratosis congenita—Update 2015. *Eur. J. Hum. Genet.*, 10.1038/ejhg.2014.170 (2015).
8. T. Vulliamy *et al.*, Mutations in the telomerase component NHP2 cause the premature ageing syndrome dyskeratosis congenita. *Proc. Natl. Acad. Sci. U.S.A.* **105**, 8073–8078 (2008).
9. M. Benyelles *et al.*, NHP2 deficiency impairs rRNA biogenesis and causes pulmonary fibrosis and Høyeraal-Hreidarsson syndrome. *Hum. Mol. Genet.* **29**, 907–922 (2020).
10. A. J. Walne *et al.*, Genetic heterogeneity in autosomal recessive dyskeratosis congenita with one subtype due to mutations in the telomerase-associated protein NOP10. *Hum. Mol. Genet.* **16**, 1619–1629 (2007).

11. T. Vulliamy *et al.*, The RNA component of telomerase is mutated in autosomal dominant dyskeratosis congenita. *Nature* **413**, 432–435 (2001).
12. A. Marrone *et al.*, Telomerase reverse-transcriptase homozygous mutations in autosomal recessive dyskeratosis congenita and Hoyeraal-Hreidarsson syndrome. *Blood* **110**, 4198–4205 (2007).
13. S. A. Savage *et al.*, TINF2, a component of the shelterin telomere protection complex, is mutated in dyskeratosis congenita. *Am. J. Hum. Genet.* **82**, 501–509 (2008).
14. T. Vulliamy *et al.*, Telomere length measurement can distinguish pathogenic from non-pathogenic variants in the shelterin component, TIN2. *Clin. Genet.* **81**, 76–81 (2012).
15. T. Vulliamy *et al.*, Disease anticipation is associated with progressive telomere shortening in families with dyskeratosis congenita due to mutations in TERC. *Nat. Genet.* **36**, 447–449 (2004).
16. M. Armanios *et al.*, Haploinsufficiency of telomerase reverse transcriptase leads to anticipation in autosomal dominant dyskeratosis congenita. *Proc. Natl. Acad. Sci. U.S.A.* **102**, 15960–15964 (2005).
17. L. Y. Hao *et al.*, Short telomeres, even in the presence of telomerase, limit tissue renewal capacity. *Cell* **123**, 1121–1131 (2005).
18. J. M. Wong, K. Collins, Telomerase RNA level limits telomere maintenance in X-linked dyskeratosis congenita. *Genes Dev.* **20**, 2848–2858 (2006).
19. Y. Bykhovskaya, K. Casas, E. Mengesha, A. Inbal, N. Fischel-Ghodsian, Missense mutation in pseudouridine synthase 1 (PUS1) causes mitochondrial myopathy and sideroblastic anemia (MLASA). *Am. J. Hum. Genet.* **74**, 1303–1308 (2004).
20. R. Shaheen *et al.*, A homozygous truncating mutation in PUS3 expands the role of tRNA modification in normal cognition. *Hum. Genet.* **135**, 707–713 (2016).
21. A. P. M. de Brouwer *et al.*, Variants in PUS7 cause intellectual disability with speech delay, microcephaly, short stature, and aggressive behavior. *Am. J. Hum. Genet.* **103**, 1045–1052 (2018).
22. S. Richards *et al.*; ACMG Laboratory Quality Assurance Committee, Standards and guidelines for the interpretation of sequence variants: A joint consensus recommendation of the American College of Medical Genetics and Genomics and the Association for Molecular Pathology. *Genet. Med.* **17**, 405–424 (2015).
23. I. Dokal, Dyskeratosis congenita in all its forms. *Br. J. Haematol.* **110**, 768–779 (2000).
24. C. Sirinavin, A. A. Trowbridge, Dyskeratosis congenita: Clinical features and genetic aspects. Report of a family and review of the literature. *J. Med. Genet.* **12**, 339–354 (1975).
25. T. J. Vulliamy, S. W. Knight, I. Dokal, P. J. Mason, Skewed X-inactivation in carriers of X-linked dyskeratosis congenita. *Blood* **90**, 2213–2216 (1997).
26. J. He *et al.*, Targeted disruption of Dkc1, the gene mutated in X-linked dyskeratosis congenita, causes embryonic lethality in mice. *Oncogene* **21**, 7740–7744 (2002).
27. B. P. Alter *et al.*, Very short telomere length by flow fluorescence in situ hybridization identifies patients with dyskeratosis congenita. *Blood* **110**, 1439–1447 (2007).
28. C. Trahan, C. Martel, F. Dragon, Effects of dyskeratosis congenita mutations in dyskerin, NHP2 and NOP10 on assembly of H/ACA pre-RNPs. *Hum. Mol. Genet.* **19**, 825–836 (2010).
29. R. Rashid *et al.*, Crystal structure of a Cbf5-Nop10-Gar1 complex and implications in RNA-guided pseudouridylation and dyskeratosis congenita. *Mol. Cell* **21**, 249–260 (2006).
30. A. C. Morris, The genetics of ocular disorders: Insights from the zebrafish. *Birth Defects Res. C Embryo Today* **93**, 215–228 (2011).
31. Y. Zhang, K. Morimoto, N. Danilova, B. Zhang, S. Lin, Zebrafish models for dyskeratosis congenita reveal critical roles of p53 activation contributing to hematopoietic defects through RNA processing. *PLoS One* **7**, e30188 (2012).
32. T. C. Pereboom, L. J. van Weele, A. Bondt, A. W. MacInnes, A zebrafish model of dyskeratosis congenita reveals hematopoietic stem cell formation failure resulting from ribosomal protein-mediated p53 stabilization. *Blood* **118**, 5458–5465 (2011).
33. M. C. Carneiro *et al.*, Short telomeres in key tissues initiate local and systemic aging in zebrafish. *PLoS Genet.* **12**, e1005798 (2016).
34. C. Bellodi *et al.*, H/ACA small RNA dysfunctions in disease reveal key roles for noncoding RNA modifications in hematopoietic stem cell differentiation. *Cell Rep.* **3**, 1493–1502 (2013).
35. M. Poulain, T. Lepage, Mezzo, a paired-like homeobox protein is an immediate target of Nodal signalling and regulates endoderm specification in zebrafish. *Development* **129**, 4901–4914 (2002).
36. G. Golling *et al.*, Insertional mutagenesis in zebrafish rapidly identifies genes essential for early vertebrate development. *Nat. Genet.* **31**, 135–140 (2002).
37. R. N. Kettleborough *et al.*, A systematic genome-wide analysis of zebrafish protein-coding gene function. *Nature* **496**, 494–497 (2013).
38. N. Danilova, K. M. Sakamoto, S. Lin, Ribosomal protein L11 mutation in zebrafish leads to haematopoietic and metabolic defects. *Br. J. Haematol.* **152**, 217–228 (2011).
39. Y. Zhang, H. Lu, Signaling to p53: Ribosomal proteins find their way. *Cancer Cell* **16**, 369–377 (2009).
40. L. Guo *et al.*, Detection of the 113p53 protein isoform: A p53-induced protein that feeds back on the p53 pathway to modulate the p53 response in zebrafish. *Cell Cycle* **9**, 1998–2007 (2010).
41. D. Ruggero *et al.*, Dyskeratosis congenita and cancer in mice deficient in ribosomal RNA modification. *Science* **299**, 259–262 (2003).
42. B. W. Gu *et al.*, Impaired telomere maintenance and decreased canonical WNT signaling but normal ribosome biogenesis in induced pluripotent stem cells from X-linked dyskeratosis congenita patients. *PLoS One* **10**, e0127414 (2015).
43. M. Kirwan, I. Dokal, Dyskeratosis congenita: A genetic disorder of many faces. *Clin. Genet.* **73**, 103–112 (2008).
44. L. Baala *et al.*, Pleiotropic effects of CEP290 (NPHP6) mutations extend to Meckel syndrome. *Am. J. Hum. Genet.* **81**, 170–179 (2007).
45. G. Matthijs *et al.*, Mutations in PMM2, a phosphomannomutase gene on chromosome 16p13, in carbohydrate-deficient glycoprotein type I syndrome (Jaeken syndrome). *Nat. Genet.* **16**, 88–92 (1997).
46. O. R. Cabezas *et al.*, Polycystic kidney disease with hyperinsulinemic hypoglycemia caused by a promoter mutation in phosphomannomutase 2. *J. Am. Soc. Nephrol.* **28**, 2529–2539 (2017).
47. O. Gribouval *et al.*, Mutations in genes in the renin-angiotensin system are associated with autosomal recessive renal tubular dysgenesis. *Nat. Genet.* **37**, 964–968 (2005).
48. M. Zivná *et al.*, Dominant renin gene mutations associated with early-onset hyperuricemia, anemia, and chronic kidney failure. *Am. J. Hum. Genet.* **85**, 204–213 (2009).
49. D. Fatkin *et al.*, Missense mutations in the rod domain of the lamin A/C gene as causes of dilated cardiomyopathy and conduction-system disease. *N. Engl. J. Med.* **341**, 1715–1724 (1999).
50. M. Eriksson *et al.*, Recurrent de novo point mutations in lamin A cause Hutchinson-Gilford progeria syndrome. *Nature* **423**, 293–298 (2003).
51. T. M. Carlile *et al.*, Pseudouridine profiling reveals regulated mRNA pseudouridylation in yeast and human cells. *Nature* **515**, 143–146 (2014).
52. X. Li *et al.*, Chemical pulldown reveals dynamic pseudouridylation of the mammalian transcriptome. *Nat. Chem. Biol.* **11**, 592–597 (2015).
53. M. Penzo, A. N. Guerrieri, F. Zacchini, D. Treré, L. Montanaro, RNA pseudouridylation in physiology and medicine: For better and for worse. *Genes (Basel)* **8**, E301 (2017).
54. D. A. Braun *et al.*, Mutations in KEOPS-complex genes cause nephrotic syndrome with primary microcephaly. *Nat. Genet.* **49**, 1529–1538 (2017).
55. D. Nachmani *et al.*, Germline NPM1 mutations lead to altered rRNA 2′-O-methylation and cause dyskeratosis congenita. *Nat. Genet.* **51**, 1518–1529 (2019).
56. G. R. Abecasis, S. S. Cherny, W. O. Cookson, L. R. Cardon, Merlin–Rapid analysis of dense genetic maps using sparse gene flow trees. *Nat. Genet.* **30**, 97–101 (2002).
57. N. Jurkute *et al.*, SSBP1 mutations in dominant optic atrophy with variable retinal degeneration. *Ann. Neurol.* **86**, 368–383 (2019).
58. J. Duan, L. Li, J. Lu, W. Wang, K. Ye, Structural mechanism of substrate RNA recruitment in H/ACA RNA-guided pseudouridine synthase. *Mol. Cell* **34**, 427–439 (2009).
59. B. Liang *et al.*, Structure of a functional ribonucleoprotein pseudouridine synthase bound to a substrate RNA. *Nat. Struct. Mol. Biol.* **16**, 740–746 (2009).
60. J. Zhou, B. Liang, H. Li, Functional and structural impact of target uridine substitutions on the H/ACA ribonucleoprotein particle pseudouridine synthase. *Biochemistry* **49**, 6276–6281 (2010).
61. B. K. Koo *et al.*, Structure of H/ACA RNP protein Nhp2p reveals cis/trans isomerization of a conserved proline at the RNA and Nop10 binding interface. *J. Mol. Biol.* **411**, 927–942 (2011).
62. S. Li *et al.*, Reconstitution and structural analysis of the yeast box H/ACA RNA-guided pseudouridine synthase. *Genes Dev.* **25**, 2409–2421 (2011).
63. J. C. Shelley *et al.*, Epik: A software program for pK(a) prediction and protonation state generation for drug-like molecules. *J. Comput. Aided Mol. Des.* **21**, 681–691 (2007).
64. S. Pronk *et al.*, GROMACS 4.5: A high-throughput and highly parallel open source molecular simulation toolkit. *Bioinformatics* **29**, 845–854 (2013).
65. A. E. Aliev *et al.*, Motional timescale predictions by molecular dynamics simulations: Case study using proline and hydroxyproline sidechain dynamics. *Proteins* **82**, 195–215 (2014).
66. T. Steinbrecher, J. Latzer, D. A. Case, Revised AMBER parameters for bioorganic phosphates. *J. Chem. Theory Comput.* **8**, 4405–4412 (2012).
67. S. Izadi, R. Anandakrishnan, A. V. Onufriev, Building water models: A different approach. *J. Phys. Chem. Lett.* **5**, 3863–3871 (2014).
68. K. Nowak *et al.*, Absence of γ-chain in keratinocytes alters chemokine secretion, resulting in reduced immune cell recruitment. *J. Invest. Dermatol.* **137**, 2120–2130 (2017).
69. G. Schay, L. Smeller, A. Tsuneshige, T. Yonetani, J. Fidy, Allosteric effectors influence the tetramer stability of both R- and T-states of hemoglobin A. *J. Biol. Chem.* **281**, 25972–25983 (2006).
70. G. Schay *et al.*, Without binding ATP, human Rad51 does not form helical filaments on ssDNA. *J. Phys. Chem. B* **120**, 2165–2178 (2016).
71. L. E. Jao, S. R. Wente, W. Chen, Efficient multiplex biallelic zebrafish genome editing using a CRISPR nuclease system. *Proc. Natl. Acad. Sci. U.S.A.* **110**, 13904–13909 (2013).
72. P. Aleström *et al.*, Zebrafish: Housing and husbandry recommendations. *Lab. Anim.*, 10.1177/0023677219869037 (2019).
73. M. Westerfield, *The Zebrafish Book: A Guide for the Laboratory Use of Zebrafish (Danio rerio)*, (University of Oregon Press, Eugene, OR, ed. 4, 2000).
74. S. Krejszeff *et al.*, Dynamic of efficiency of MS-222 as an anaesthetic for tench *Tinca tinca* (L.) larvae. *Commun. Agric. Appl. Biol. Sci.* **78**, 227–230 (2013).
75. E. Mishima *et al.*, Immuno-Northern blotting: Detection of RNA modifications by using antibodies against modified nucleosides. *PLoS One* **10**, e0143756 (2015).
76. P. J. Cock, C. J. Fields, N. Goto, M. L. Heuer, P. M. Rice, The Sanger FASTQ file format for sequences with quality scores, and the Solexa/Illumina FASTQ variants. *Nucleic Acids Res.* **38**, 1767–1771 (2010).
77. M. Pertea, D. Kim, G. M. Pertea, J. T. Leek, S. L. Salzberg, Transcript-level expression analysis of RNA-seq experiments with HISAT, StringTie and Ballgown. *Nat. Protoc.* **11**, 1650–1667 (2016).
78. G. Yu, L. G. Wang, Y. Han, Q. Y. He, clusterProfiler: An R package for comparing biological themes among gene clusters. *OMICS* **16**, 284–287 (2012).
79. G. la Marca *et al.*, Implementing tandem mass spectrometry as a routine tool for characterizing the complete purine and pyrimidine metabolic profile in urine samples. *J. Mass Spectrom.* **41**, 1442–1452 (2006).